

## Article

# Numerical and Experimental Study on Large-Diameter FRP Cable Anchoring System with Dispersed Tendons

Jingyang Zhou <sup>1,2</sup> , Xin Wang <sup>1,2,\*</sup> , Lining Ding <sup>3</sup>, Shui Liu <sup>1,2</sup> and Zhishen Wu <sup>1,2</sup><sup>1</sup> Key Laboratory of C & PC Structures Ministry of Education, Southeast University, Nanjing 211189, China<sup>2</sup> National and Local Unified Engineering Research Center for Basalt Fiber Production and Application Technology, International Institute for Urban Systems Engineering, Southeast University, Nanjing 211189, China<sup>3</sup> School of Civil Engineering, Nanjing Forestry University, Nanjing 210037, China

\* Correspondence: xinwang@seu.edu.cn; Tel.: +86-136-1151-4436

**Abstract:** Based on a previously designed variable-stiffness load transfer component (LTC), a novel dispersed-tendon cable anchor system (CAS) was developed to increase the anchoring efficiency of large-diameter basalt-fiber-reinforced polymer (BFRP) cables. The static behaviors of the CAS are then numerically evaluated by a simplified three-dimensional finite-element (FE) model and implemented in a full-scale BFRP cable. The FE results indicated that the accuracy of the simplified dispersed-tendon model could be effectively ensured by dividing the revised compensation factor. The anchor behavior of the dispersed-tendon CAS was superior to that of the parallel-tendon CAS when the same cable was applied. The radial stress and tensile stress difference can be reduced by decreasing the tendon spacing. The testing and simulated results agreed well with the load–displacement relationship and axial displacement. All tendons fractured in the testing section, and the LTC suffered minimal damage. The ultimate force of the cable with 127 4-mm-diameter tendons was 2419 kN, and the corresponding anchoring efficiency was 93%. The cable axial tensile strain in the anchoring zone decreased linearly from the loading end to the free end. The cable shear stress concentration at the loading end can be avoided by employing a variable-stiffness anchoring method.



**Citation:** Zhou, J.; Wang, X.; Ding, L.; Liu, S.; Wu, Z. Numerical and Experimental Study on Large-Diameter FRP Cable Anchoring System with Dispersed Tendons. *Buildings* **2023**, *13*, 92. <https://doi.org/10.3390/buildings13010092>

Academic Editor: Elena Ferretti

Received: 21 November 2022

Revised: 26 December 2022

Accepted: 27 December 2022

Published: 30 December 2022



**Copyright:** © 2022 by the authors. Licensee MDPI, Basel, Switzerland. This article is an open access article distributed under the terms and conditions of the Creative Commons Attribution (CC BY) license (<https://creativecommons.org/licenses/by/4.0/>).

**Keywords:** basalt-fiber-reinforced polymers (BFRP); larger-diameter cable; dispersed-tendon anchoring method; finite-element (FE) analysis; full-scale experiment

## 1. Introduction

Fiber-reinforced polymers (FRPs) have many outstanding features [1–3], such as light weight, high tensile strength, and corrosion resistance. FRPs are frequently considered ideal materials for solving the bottleneck problems of steel cables [4–6], including easy corrosion and considerable weight. The application of FRP cables in civil engineering has gradually increased [7–9]. Generally, carbon FRP (CFRP) cables are used as partial or full structural members to strengthen engineering structures [10–12]. For example, a network arch bridge with a 124 m span was built across a highway in Stuttgart, Germany, in 2020. All the hangers were created from CFRP. CFRP hangers have many advantages over steel hangers [13], such as a small cross-section, low cost, long service life, and flexible aesthetic arrangement. In another case, a highway cable-stayed bridge having two 100 m main spans, supported by sixty-eight steel cables and four CFRP cables, was successfully built in Shandong, China, in 2022. The CFRP cable was manufactured using 121 7 mm-diameter tendons. The mean ultimate load was 10,440 kN. The mean anchoring efficiency, denoted as the ratio of the measured ultimate to the standard value of the tensile load of the cable, was 107%. Recently, a self-anchored CFRP cable, developed by Feng et al. [14], was applied in steel trusses in Shanghai, China, in 2022. The ultimate load of the cable reached 4550 kN.

In summary, an increasing number of engineering applications indicates that CFRP cables are becoming competitive substitutes for traditional steel cables [15–19].

However, CFRP cables also have some limitations [20], such as high price, brittle fracturing, and low ductility; thus, their application range is limited to some extent. High-performance structural materials should be developed to fill the application blank zone of CFRP cables. Compared with CFRP, basalt FRP (BFRP) is a recently emerging prestressing material [21–23]. BFRP materials are primarily used to enhance new structures and reinforce existing structures owing to their outstanding characteristics, such as high creep fracture stress, high ductility, high performance–price ratio, and eco-friendliness [24]. However, the elastic modulus of BFRPs is significantly lower than those of CFRPs and steel [25]. Consequently, the tensile deformation of BFRP cables is inevitably larger than that of CFRP and steel cables, resulting in excessive deformation of the structures supported by cables. The development of large-diameter BFRP cables is frequently considered an effective solution to solving this problem. However, the anchoring efficiency of BFRP cables also decreases with an increase in cable diameter. Therefore, the premise of utilizing large-diameter BFRP cables is to increase their anchoring efficiency.

Many anchoring methods for FRP cables were proposed by using different inner shape in steel anchorages and designing novel load transfer components (LTCs) [26], but few were adapted to large-diameter BFRP cables. For instance, Wang [27] developed a sectional LTC composed of different continuous fibers and epoxy resin to decrease the stress concentration of BFRP cables with 37 4-mm-diameter tendons. The mean tensile load and anchor efficiency of the BFRP cables were 592 kN and 99%, respectively. Shi [28] developed a composite-wedge anchorage for BFRP tendons involving three variable-stiffness wedges composed of resin, impregnated chopped fiber, silica sand, and fiber sheet. The anchor efficiency and fatigue cycle of the cable anchor system (CAS) were 91% and more than 200 million cycles, respectively. Compared with existing CFRP cables, the proposed methods are most suitable for small-diameter BFRP cables. In summary, there is an urgent need to develop anchoring methods for large-diameter BFRP cables.

In a previous study [29], a sectional variable-stiffness LTC fabricated with epoxy resin and chopped glass fibers with a length of 900  $\mu\text{m}$  and a diameter of 13  $\mu\text{m}$  was proposed (Figure 1). The fiber volume fractions of the segmented LTCs, defined as the volume ratio of fiber to fiber and epoxy resin, were 0%, 8.9%, 22.8%, and 40% [30], respectively. The corresponding elastic moduli were 2.8, 5.17, 7.53, and 9.9 GPa [30], respectively. The anchor-zone cable was arranged in parallel, and the tendon spacing was 1.5 mm. The lengths of the sectional LTCs were 115 (containing a horizontal segment of 15 mm), 100, 100, and 100 mm, respectively. Through full-scale experiments, the mean ultimate tensile load and anchoring efficiency of the three BFRP cables were observed to be 1919 kN and 95% [30], respectively. The proposed method was preliminarily verified to be suitable for anchoring large-diameter cables. However, the anchoring efficiency tends to decline, and the coil radius of the cable increases when the cable diameter exceeds a specific limit. To solve the problems, the cable arrangement in the anchoring zone can be changed from parallel to dispersed. The improvement effect of the method on anchoring efficiency was verified in a previous study on CFRP cables composed of 37 7-mm-diameter tendons [30]. The tensile strength of the CFRP cables exceeded 3000 MPa. The principle of improvement is to use the dispersed tendons to bear part of the axial shear force to avoid shear failure in the LTC. In addition, the coil radius of the cable can be decreased by reducing the tendon spacing and diameter.

As shown in Figure 2, a novel anchoring method was further proposed based on the above optimization strategy. Compared with the previous CAS shown in Figure 1, only the tendon diameter, tendon number, and arrangement of the BFRP cable were changed. The anchorage was derived from a previous experiment, and the sectional LTCs were also unchanged. The BFRP cable was composed of 127 4-mm-diameter tendons in a regular hexagonal arrangement. From the center layer to the outermost layer, the bending angles of the tendons, denoted as the arctangent of the ratio of tendon transverse deviation distance



room temperature. An extensometer with a gauge length of 50 mm was used to measure the tensile strain of the BFRP tendon.

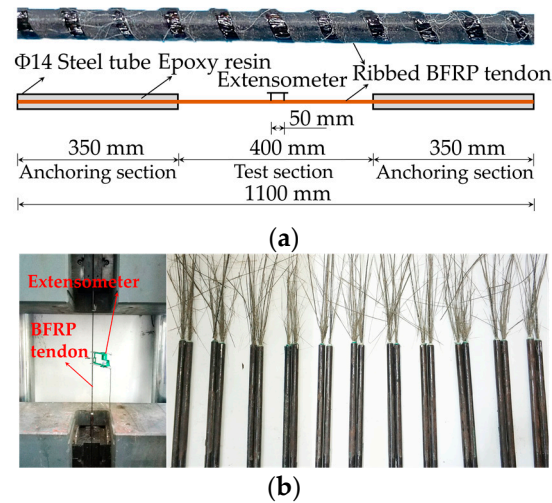


**Figure 3.** Tensile test of BFRP tendons: (a) anchoring scheme and (b) loading and failure.

## 2.2. Calculation Method

The tensile properties of the BFRP tendons can be calculated according to Chinese Standard (GB/T 30022–2013) [32]. The equations are listed in Equations (1)–(4). Specifically,  $\sigma_u$  is the tensile strength (MPa).  $F_u$  is the ultimate tensile load (kN).  $A_{st}$  is the cross-sectional area ( $\text{mm}^2$ ).  $E_L$  is the elastic modulus (GPa).  $\varepsilon_u$  is the ultimate tensile strain ( $\mu\text{e}$ ).  $\varepsilon_1$  and  $\varepsilon_2$  are the tensile strains when the loads are  $F_1$  and  $F_2$ , respectively.  $F_1$  and  $F_2$  are 20% and 50% of  $F_u$ , respectively.  $f_{fpk}$  is the standard value of  $\sigma_u$ , which considers the dispersion of BFRP materials and 95% strength assurance rate [30].  $f_a$  is the average  $\sigma_u$ .  $\sigma$  is the standard deviation (SD) of  $\sigma_u$ . The coefficient of variation (CV) is the ratio of  $\sigma$  to  $f_a$ .

$$\sigma_u = \frac{F_u}{A_{st}} \quad (1)$$

$$E_L = \frac{F_1 - F_2}{(\varepsilon_1 - \varepsilon_2)A_{st}} \quad (2)$$

$$\varepsilon_u = \frac{F_u}{E_L A_{st}} \quad (3)$$

$$f_{fpk} = f_a(1 - 1.645CV) = f_a - 1.645\sigma \quad (4)$$

## 2.3. Results and Discussions

As shown in Figure 3b, a universal machine with a loading capacity of 2000 kN was employed for the BFRP tendons. A tensile speed of 2 mm/min was determined to obtain the elastic modulus of the BFRP tendons according to the standard [32]. In the loading process, the tensile force increased linearly with piston displacement, verifying the linear elastic property of the BFRP tendon. Fiber breakage began to occur gradually when the tensile force exceeded 80% of the ultimate load. The final fracture of the BFRP tendons was abrupt with hardly a warning. All the specimens exhibited a typical multifilament fracture at the test section, indicating that the anchoring scheme was effective and that the material strength was utilized entirely.

The experimental results for the BFRP tendons are displayed in Table 1, in which  $\sigma_u$ ,  $F_u$ ,  $E_L$ ,  $\varepsilon_u$  and  $f_{fpk}$  were calculated by Equations (1)–(4). The mean values of  $\sigma_u$ ,  $F_u$ ,  $E_L$ , and  $\varepsilon_u$  were 21 kN, 1702 MPa, 55 GPa, and 3.11%, respectively, which were superior to the tensile performance of BFRP tendons in [27]. In addition, the CVs of the tendons were less than 4%, indicating that the tendons with low material dispersion can be employed as

prestressing cable members. According to Equation (4), the  $f_{fpk}$  of the eleven BFRP tendons was 1638 MPa, which was the basis for calculating the standard value of the ultimate tensile force of the multi-tendon BFRP cable in the following analysis.

**Table 1.** Testing results for the BFRP tendons.

Specimen	$F_u$ /kN	$\sigma_u$ /MPa	$E_L$ /MPa	$\varepsilon_u$ /%
1	22	1715	54	3.16
2	21	1689	55	3.06
3	21	1707	54	3.14
4	21	1709	54	3.14
5	21	1654	55	2.99
6	22	1754	53	3.28
7	21	1678	55	3.04
8	20	1625	55	2.94
9	22	1726	55	3.12
10	22	1764	54	3.25
11	21	1697	55	3.07
Mean	21	1702	55	3.11
SD	0.48	38.53	0.61	0.10
CV/%	2.26	2.26	1.12	3.16

### 3. Simulation Analysis of the Dispersed-Tendon CAS

#### 3.1. Proposal of the Simplified Model

##### 3.1.1. Shortcomings of the Full Model

A 3D FE model (called the full model) for parallel-tendon CAS with 37 7-mm-diameter BFRP tendons was created using the ABAQUS/Standard program and C3D8R elements to simulate actual experiments with high accuracy in the previous study [30] (see Figure 4). The full model is characterized by the ability to consider the existence of multiple independent FRP tendons. The accuracy of the full model was verified to be high compared with previous experimental results [29,33]. However, the full model also contributed to an excessive computing burden resulting from the rapidly increasing number of elements and convergence challenges [31]. Additionally, meshing of the full model used for dispersed-tendon CAS was significantly tricky because of the irregular inner geometric shape of the LTC and dispersed tendons. Therefore, a simplified 3D FE model is required to make the calculation and meshing more feasible.

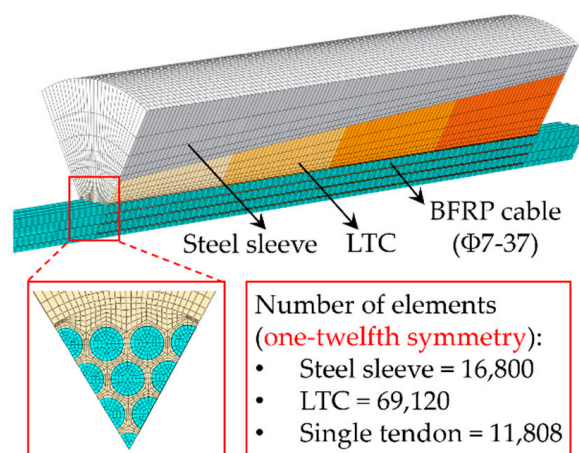


**Figure 4.** Full FE model.

##### 3.1.2. Theoretical Analysis for the Simplified Model

In a previous study [31], a simplified model for parallel-tendon CAS was proposed using Ansys 15.0 and Solid 186 elements (Figure 5). The simplified model was characterized

by the ability to replace multiple tendons with several rings. However, the disadvantages of the simplified model deserve attention. The equivalent ring model has a ring hoop effect. The ring cable will generate circumferential resistance when subjected to radial extrusion. Thus, the deformation of the cable was limited. This deformation characteristic is completely different from that of the multiple-tendon cable. In this model, the tendons in each layer are equivalent to the corresponding concentric rings based on the principle of equal cross-sectional areas. The center tendon is defined as the first ring. The radius and thickness  $t$  of the  $i$ th ring are expressed as Equations (5) and (6), where  $D_t$  is the tendon diameter (mm),  $\delta$  is the tendon spacing (mm), and  $N(i)$  is the number of tendons in the  $i$ th layer. For a regular hexagonal arrangement,  $N(i) = 1, 6, 12, 18 \dots$ , for  $i = 1, 2, 3, 4 \dots$ , respectively [31].

$$R^{center}(i) = (i - 1)(D_t + \delta) \quad (5)$$

$$t(i) = R^{outer}(i) - R^{inner}(i) = \frac{N(i)D_t^2}{8R^{center}(i)} \quad (6)$$

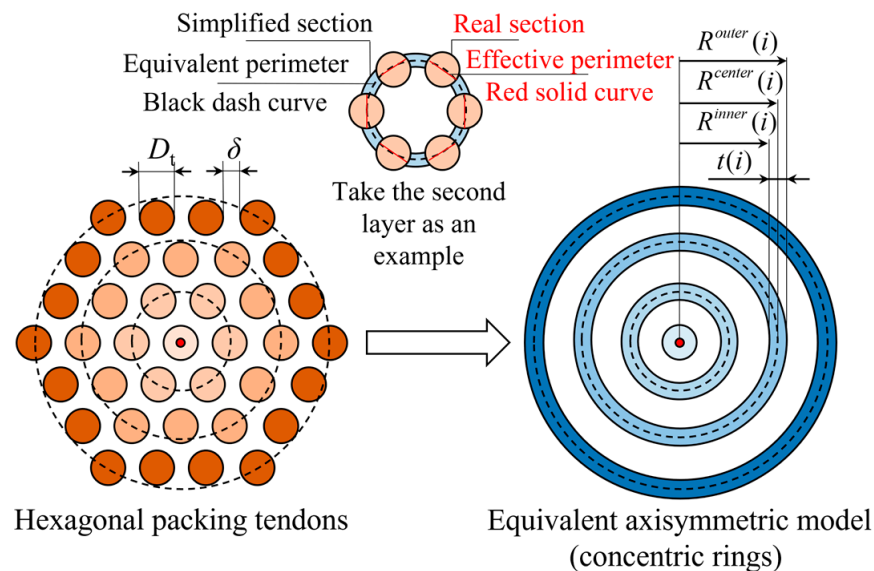


**Figure 5.** Simplification of the parallel-tendon cable.

Based on this assumption, the radial and shear stress of BFRP cables were consistently underestimated owing to the absence of tendon spacing. Therefore, a compensation factor  $\varphi$ , defined as the ratio of the effective perimeter of the real section to that of the simplified section [31] (see Figure 5), was proposed. When  $i \geq 2$ ,  $\varphi$  can be expressed as Equation (7), where  $\varphi$  is a constant when  $i \geq 2$ . This phenomenon can be explained by the constant wall thickness of the rings in the axial direction. The radial and shear stresses of the BFRP cable, obtained from the simplified FE model with parallel concentric rings along the axial direction, can be further adjusted by dividing  $\varphi$ . However, for the dispersed-tendon CAS, the derived  $\varphi$  cannot be employed directly because of the varying wall thickness of the rings along the axial direction. Thus,  $\varphi$  must be further revised to be consistent with the full dispersed-tendon model.

$$\varphi(i) = \frac{N(i)D_t}{2\pi R^{center}(i)} = \frac{N(i)D_t}{2\pi(i - 1)(D_t + \delta)} \quad (7)$$

As shown in Figure 6, the geometric shape of the dispersed tendons in the  $i$ th layer can be regarded as an arc. According to the geometrical relationship,  $y(i)$  and  $R^{center}(i)$  can be expressed as Equations (8)–(10). Specifically,  $L$  is the anchoring length.  $\theta(i)$  is the bending angle of the dispersed tendons in the  $i$ th layer.  $R(i)$  is the bending radius of the dispersed tendons in the  $i$ th layer.  $x(i)$  is the horizontal distance between the point in the center position of the  $i$ th layer and the loading end.  $y(i)$  is the vertical distance between the point in the center

position of the  $i$ th layer and the center line of the first layer. Based on Equations (8)–(10), Equation (7) can be revised as Equation (11). Based on the given dispersed-tendon CAS in Figure 2, the following parameters can be determined:  $D_t = 4$  mm,  $L = 415$  mm, and  $\theta(i) = 0^\circ, 0.75^\circ, 1.5^\circ, 2.25^\circ, 3^\circ, 3.75^\circ, 4.5^\circ$ , for  $i = 1, 2, 3, 4, 5, 6, 7$ , respectively.

$$R(i) = \frac{L}{2 \sin \theta(i) \cos \theta(i)} \quad (8)$$

$$y(i) = R(i) - \sqrt{R(i)^2 - x(i)^2} \quad (9)$$

$$R^{center}(i) = (i-1)(D_t + \delta) + y(i) \quad (10)$$

$$\varphi = \frac{N(i)D_t}{2\pi \left[ (i-1)(D_t + \delta) + \frac{L}{2 \sin \theta(i) \cos \theta(i)} - \sqrt{\left( \frac{L}{2 \sin \theta(i) \cos \theta(i)} \right)^2 - x(i)^2} \right]} \quad (11)$$

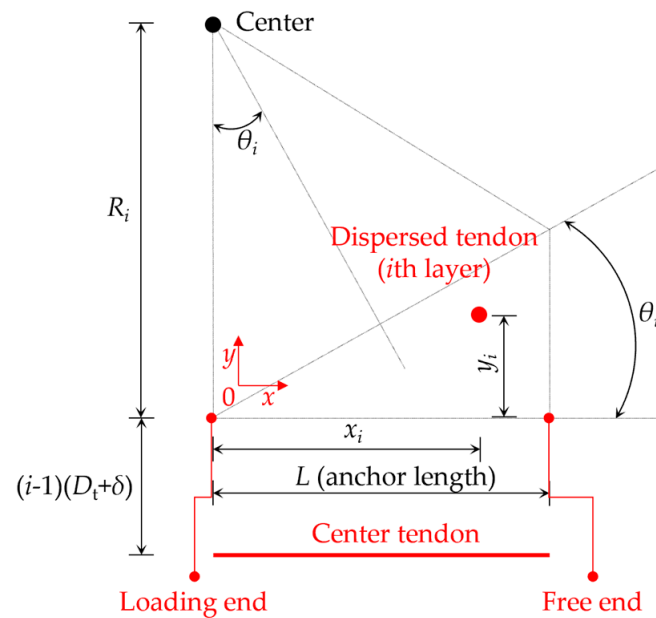


**Figure 6.** Geometric relation of dispersed tendons.

### 3.2. FE Modeling

For the proposed CAS shown in Figure 2, the tendon spacing was first determined based on a parallel-tendon model. The advantage of using a parallel-tendon model is that it can fully consider the influence of the change in tendon spacing on cables in different positions. Subsequently, the superiority of the dispersed tendon was verified by comparing it with the parallel-tendon CAS based on the full and simplified models. According to the symmetry of the CAS having 127 4-mm-diameter tendons, three types of FE models, namely full parallel-tendon, simplified parallel-tendon, and simplified dispersed-tendon models, were established based on ABAQUS/Standard (Figure 7). The number of elements along the part thickness direction is not less than three. Based on the same meshing principles, the 1/12 full FE model includes 121,968 elements for cable and 30,840 elements for LTC. In comparison, the 1/12 simplified FE model includes only 44,604 elements for cable and 24,840 elements for LTC. Thus, the total number of elements can be dramatically reduced through simplifying. The detailed dimensions of the anchorage and the LTC are shown in Figure 2.

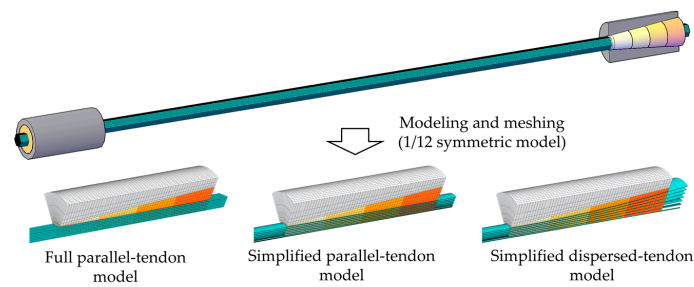


**Figure 7.** Full and simplified FE models.

A friction coefficient of 0.15 at the interface of the LTC and the anchorage was set based on previous simulations [26,29]. The interaction between the outer surfaces of the cable and the inner surfaces of the LTC was considered a tie because of sufficient cohesive action. The symmetric model was implemented by applying cyclic symmetry constraints to two symmetric planes and axial symmetry constraints to the cross-section of the cable at the middle portion. The eight-node solid element C3D8R was selected for the entire model to obtain high simulation accuracy [30]. A concentrated load was applied to the reference point, which was coupled to the surface of the anchorage perpendicular to the tensile direction of the cable. Based on  $f_{fpk}$  and the nominal diameter of the tendons, the load for the 1/12 model was 435,346 N. The material properties of the FE model critically affect the accuracy of the simulation and the convergence of the model. Only linear elasticity was employed in the simulation process to reveal the stress distributions and deformations of the CAS. The mechanical properties of the BFRP CAS that were obtained from Table 1 and previous studies are listed in Table 2, where some data derived from Wang et al. [34] and Zhou et al. [30] were used to create the table.

**Table 2.** Model parameters for the BFRP CAS.

Property		Cable	LTC	Sleeve
Poisson's ratio	Major	0.30	0.3	0.3
	Minor	0.02	0.3	0.3
Elasticity modulus (GPa)	Longitudinal	55	2.8–9.9	200
	Transverse	8	2.8–9.9	200
Shear modulus (GPa)	Longitudinal	6.0	/	77
	Transverse	6.0	/	77
Tensile strength (MPa)	Longitudinal	1702	/	560
	Transverse	/	/	560
Compressive strength (MPa)	Transverse	143	85–125	540
Elongation (%)	Longitudinal	3.11	/	>4

### 3.3. Simulated Results and Discussions

#### 3.3.1. Determination of Tendon Spacing

Four tendon spacings (0, 0.5, 1, and 1.5 mm) were studied using a full parallel-tendon FE model. In a previous study, an apparent stress concentration in the outermost tendons at the sharp corners was observed. Thus, tendon-127 (T-127) was selected for further analysis. As shown in Figure 8a, the tendon spacing had a slight effect on the axial tensile stress of T-127, primarily attributed to the higher tensile elastic modulus of the BFRP tendons than that of the LTC. As shown in Figure 8b, the tensile stress difference between the inside and outside ( $\Delta\sigma$ ) of T-127 and the radial compressive stress reached a maximum value near the loading end. The  $\Delta\sigma$  of T-127 near the loading end also increased with an increase in tendon spacing, primarily caused by the tension-bending deformation of the tendon. The tensile stress difference between the inside and outside of the tendons decreased by 38%. The radial compressive stress in Figure 8c exhibited variation characteristics similar to  $\Delta\sigma$ . The loading-end radial stress decreased by 12% when the tendon spacing decreased from 1.5 mm to 0. In summary, the overall stress distributions of the cable in the anchoring

zone (except for the loading end) were slightly influenced by the change in tendon spacing. A tendon spacing of 0 mm was selected to minimize the diameter and bending radius of the BFRP cable.

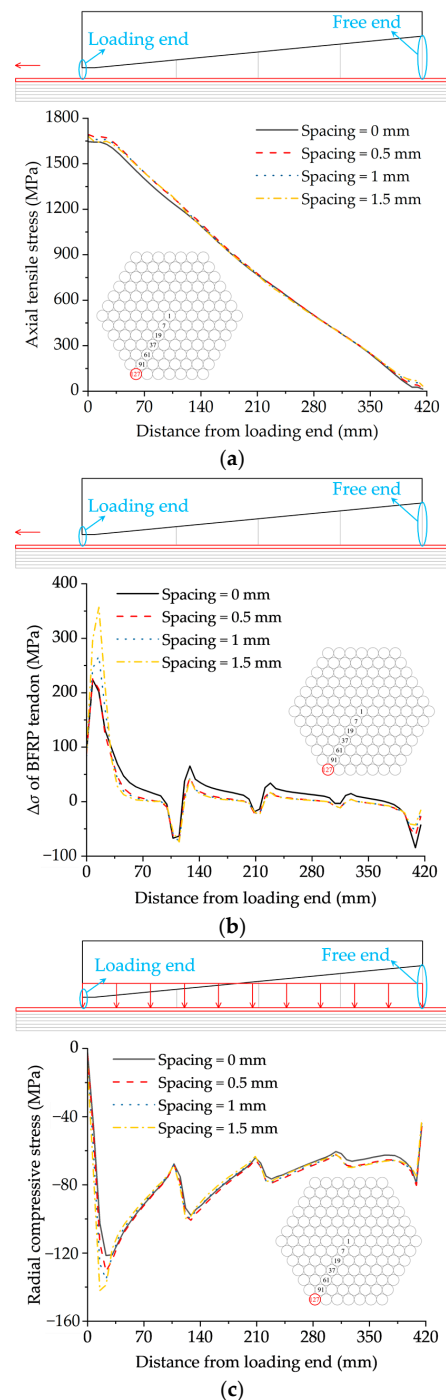


**Figure 8.** Simulated results of full model with tendon spacing: (a) axial tensile stress, (b)  $\Delta\sigma$  of BFRP tendon, and (c) radial compressive stress.

### 3.3.2. Comparison of Three Simulation Methods

A previous study indicated that the anchoring efficiency of the CFRP cables' high-strength CFRP tendons could be significantly improved by turning parallel tendons into dispersed tendons in the anchoring zone [30]. Thus, parallel-tendon and dispersed-tendon CASs were implemented to anchor the BFRP cable with a tendon spacing of 0. Full and simplified models to simulate the parallel-tendon CAS were employed to illustrate

the effectiveness of the simplified method. Although the computing time of the model is greatly affected by the computer performance, the proportion of computing time of different models on the same computer should be relatively fixed. For this simulation, the calculation time of 263 min for the full parallel-tendon model was larger than that of 47 min for the simplified one. The calculation efficiency of the simplified model was significantly higher than that of the full model.

As shown in Figure 9a, the axial tensile stress of T-1 in the centralized position was studied using different anchoring methods. From the loading end to the free end, the axial tensile stress decreased with a nearly linear trend. It was slightly influenced by the anchoring and modeling methods, which was consistent with the simplified concept. As shown in Figure 9b, the radial compressive stress of T-127 in the simplified parallel-tendon model was close to that of T-127 in the full parallel-tendon model. This phenomenon indicated that the accuracy of the radial compressive stress of the simplified parallel-tendon model can be increased by dividing the compensation factor  $\varphi$ . When the distance from the loading end exceeded 120 mm, the radial compressive stress in the simplified dispersed-tendon model was lower than that in the simplified parallel-tendon model. This phenomenon can be explained by the gradual increase in tendon spacing from the loading end to the free end because of the bending arrangement, thereby resulting in reduced extrusion action between the tendons. The large longitudinal elastic modulus difference between the cable and LTC also contributed to this result.

As shown in Figure 9c, the shear stress difference between the full and the simplified parallel-tendon models gradually decreased from the loading end to the free end. It can be explained by stress concentration and magnitude. The shear stress in the simplified parallel-tendon model was the mean value because of the symmetric circular section. However, T-127 in the full parallel-tendon model was located at the stress concentration position, resulting in excessive shear stress. Additionally, the shear stress decreased with fluctuations. Consequently, the shear stress difference between the two models decreased as the shear stress decreased. The shear stress in the simplified dispersed-tendon model was also lower than that in the simplified parallel-tendon model. This result can be explained by the fact that the farther the shear stress is from the center of the cable, the smaller the shear stress. A similar conclusion was obtained in a previous study on high-strength CFRP CAS [30].

In summary, the dispersed-tendon CAS was superior to the parallel-tendon CAS when the same cable was anchored. Meanwhile, it is feasible to use a simplified dispersed-tendon model to simulate dispersed-tendon CAS. Further simulation verification of the simplified dispersed-tendon model using a full-scale experiment will be implemented in the following study.

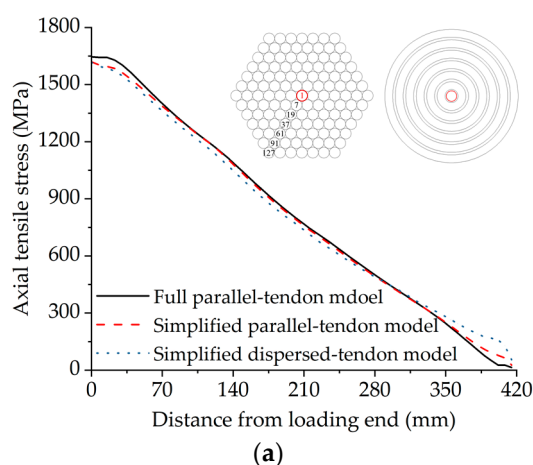
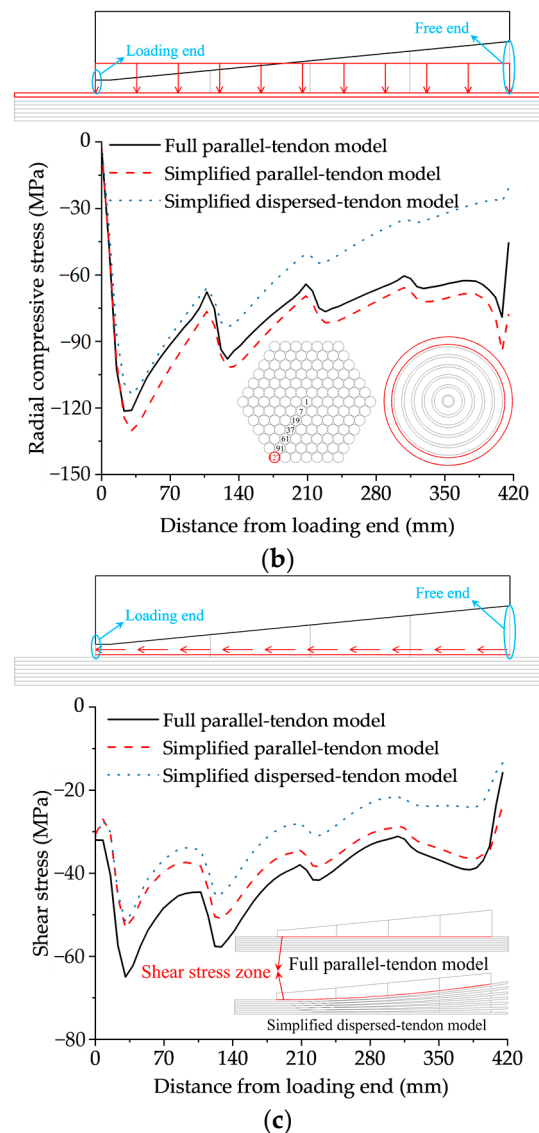


Figure 9. Cont.



**Figure 9.** Simulated results of three FE models: (a) axial tensile stress of T-1, (b) radial compressive stress of T-127, and (c) shear stress of the LTC.

## 4. Experimental Verification in Dispersed-Tendon CAS

### 4.1. Manufacturing

In the manufacturing process, the combination of the cable in the test section and the dispersion of the cable in the anchoring zone are two major challenges. Only one BFRP cable was fabricated owing to the high cost and difficulty of cable preparation. As shown in Figure 10, the cable, characterized by a tendon spacing of 0 and a regular hexagon section, was first combined by hand with two positioning plates having a hole spacing of 2 mm [33]. The assembled parts of the cable were then fixed by wrapping them with medical tape that had the advantages of toughness and viscosity at specific intervals. The test section of the cable was further compressed by wrapping it with polyethylene (PE) tape with a width of 50 mm. Subsequently, cable dispersion was realized using separate and integral polyvinyl chloride (PVC) positioning plates. Separate PVC positioning plates with a hole diameter of 4.2 mm and thickness of 2 mm were first employed to disperse the anchoring-zone cable layer by layer. The combined cable was then placed into the prepared anchorages, which were connected using two channel steel with a length of 3150 mm. Notably, the inner surfaces of the anchorages were coated with silicon grease to make removing the LTC easier after loading. The separate positioning plates were removed after all tendons

were threaded into the holes of the integrated positioning plate. The segmented LTCs were cast along the vertical direction, segment by segment. The casting interval was determined to be approximately 2 h to ensure reliable bonding between the interfaces of the adjacent LTCs. The casted LTCs were set to rest for 7 d to cure the epoxy resin adequately.

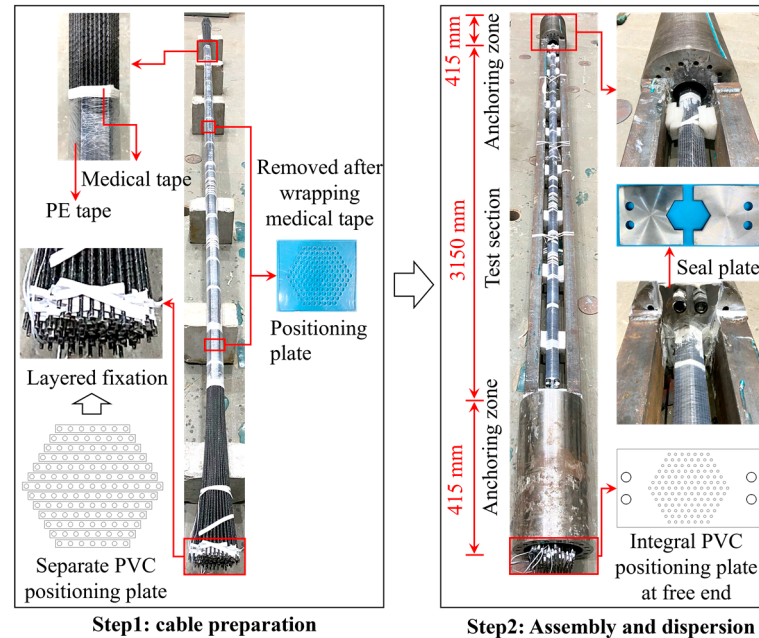


**Figure 10.** Preparation of dispersed-tendon CAS.

#### 4.2. Loading and Measuring

A horizontal stretching device with a maximum loading capacity of 6500 kN was used for tensile testing of the cable (Figure 11a). The active anchorage was connected to the load cell by a nut and 20 high-strength bolts. A steel base plate was placed between the die anchorage and bearing plate. The maximum stroke of the piston rod was 400 mm. To eliminate the assembly clearance of the loading device, a tensile force of about 5 kN to the cable to produce a pretension was applied. A graded loading method including four stages was implemented at 100 MPa/min loading speed according to the Chinese standard [35]. The load was maintained for no less than 10 min when it reached 20%, 40%, and 60% of the standard value of the ultimate tensile force of the cable.

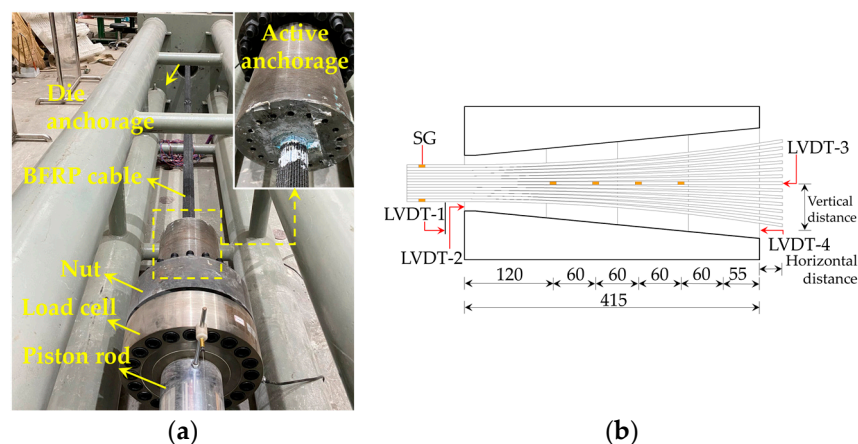


**Figure 11.** Loading and measurement schemes: (a) loading device and (b) measurement arrangement.

The measurement arrangement of the displacement and strain is shown in Figure 11b. The cable axial tensile strains at the test section and anchoring zone were collected using

eighteen and four strain gauges (SGs), respectively. The ultimate measurement range of the SGs was  $20,000 \mu\epsilon$ . The distance between SGs in the anchoring zone was set to 60 mm. The cable and LTC axial displacements at the loading and free ends were measured by four linear variable differential transformers (LVDTs) with an ultimate measuring range of 100 mm. The data acquisition frequency was 1 Hz.

#### 4.3. Experimental Results and Discussions

##### 4.3.1. Failure Mode

During the loading process, slippage of the LTC along the axial direction was observed, resulting from the smooth inner surface of the anchorage. When the load exceeded approximately 80% of the standard value of the ultimate tensile force of the cable, the external fibers of the BFRP tendons began to rupture at random. When the ultimate load was reached, several BFRP tendons in the test section began to rupture one after another. Subsequently, the remaining tendons ruptured within a short time. The uneven stress of the tendons caused this phenomenon at the test section. The final failure mode of the cable is shown in Figure 12. The LTCs in the die and active anchorages suffered slight damage, indicating that the shear and compressive strengths of the LTCs were sufficient to anchor the cable. The cable cross-sections at the loading end also indicated that the bonding between the interface of the LTC and the cable was reliable. Almost no radial extrusion damage occurred to the loading-end cable, indicating that the variable-stiffness LTC could effectively reduce the cable radial stress concentration.



**Figure 12.** Failure mode of the CAS.

##### 4.3.2. Load–Displacement Curve

As shown in Figure 13, the experimental load–displacement curve increased linearly with several fluctuations resulting from the slippage of the LTC. A horizontal section was then clearly observed at the end of the curve because of the rupture of a few tendons, demonstrating that the BFRP CAS had certain ductility characteristics. This phenomenon is mainly caused by the relatively low elastic modulus and high fracture elongation of the cable. Finally, the curve decreased rapidly after reaching an ultimate load of 2419 kN, which was significantly larger than the mean ultimate load of 1919 kN tested in a previous study [29]. Additionally, the experimental curve was followed closely by the simulated curve, indicating that the load–displacement relationships can be adequately simulated using the simplified dispersed-tendon model with high accuracy.

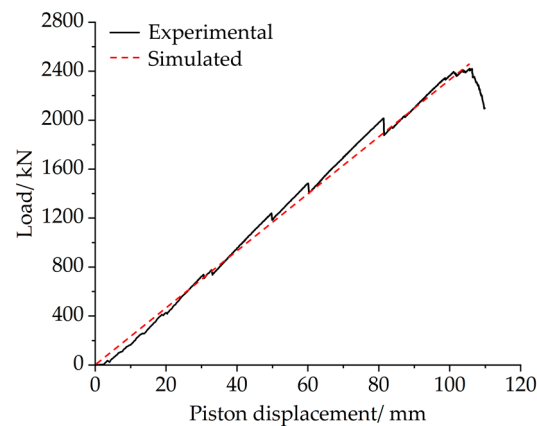


**Figure 13.** Load–displacement curve of the cable.

#### 4.3.3. Anchoring Efficiency

The anchoring efficiency defined in Equation (12) [30] is typically employed to evaluate the bearing capacity of CASs.  $\eta_a$  is the anchoring efficiency,  $F_{fTu}$  is the measured ultimate tensile load of the cable,  $F_{fpk}$  is the standard value of the ultimate tensile force of the cable, and  $N$  is the number of tendons. According to Table 1 and the cable configuration,  $f_{fpk}$ ,  $A_{st}$ , and  $N$  of the BFRP cable were 1638 MPa, 12.56 mm<sup>2</sup>, and 127, respectively.  $F_{fpk}$  was calculated to be 2613 kN.  $\eta_a$  of the CAS was calculated to be 93%, slightly lower than the 95% specified by the standard [35]. This result can be explained by several potential reasons, such as the anchorage (no redesign), assembly errors, and material dispersion.

$$\eta_a = \frac{F_{fTu}}{F_{fpk}} = \frac{F_{fTu}}{f_{fpk} A_{st} N} \quad (12)$$

#### 4.3.4. Axial Displacement

As shown in Figure 14, the experimental displacement at the loading end was noticeably larger than that at the free end, which was caused by the tensile deformations of the cable and LTC. Meanwhile, the experimental displacements of the cable were always larger than those of the LTC, which can be explained by the vertical distance difference between the LVDTs and the axial deformations of the cable and LTC. Additionally, the maximum difference between the simulated and experimental displacements was only 0.4 mm, indicating that the axial displacement can be reasonably simulated using the simplified dispersed-tendon model.

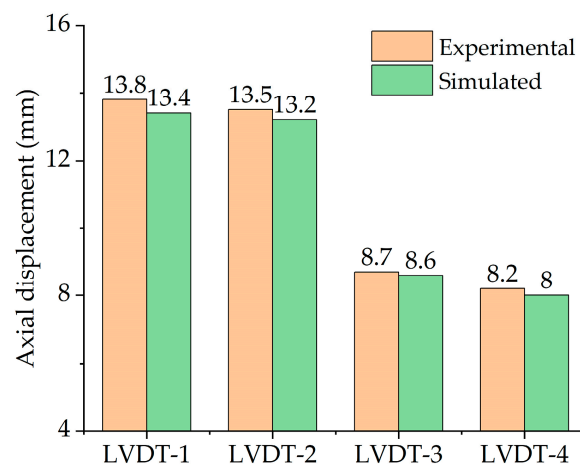


**Figure 14.** Axial displacement of the LTC and cable.

#### 4.3.5. Axial Tensile Strain

The axial tensile strains of the BFRP tendons in the outermost layer arranged at intervals were measured (Figure 15). Generally, the tensile strain of the tendons increased linearly with an increase in the load, which was in good agreement with the linear elastic characteristic of BFRP materials. The tensile strain differences between the tendons increased with increasing load, and the maximum value reached  $2551 \mu\epsilon$  when the load was 1756 kN. This phenomenon may be explained from three aspects: the length difference of tendons caused by cutting error and different initial bending shapes of tendons, the unparallel measuring direction of SGs, and the varying thicknesses of glue between tendons and SGs.

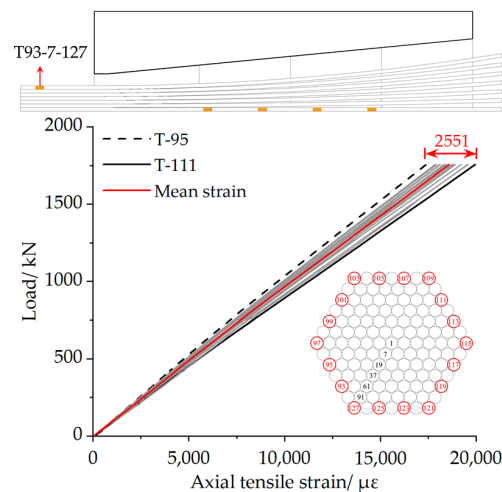


**Figure 15.** Axial tensile strains of the BFRP cable in the test section.

The changing laws of the axial tensile strains of T-1 at different load grades are shown in Figure 16, where  $D$  represents the distance from the loading end. Linear decreasing trends in the axial tensile strains of T-1 were observed at different load grades owing to the high longitudinal elastic modulus ratio of the BFRP cable to the LTC. The ratio of the maximum to minimum tensile strains generally increased with an increase in the load, primarily resulting from the axial wedge action of the LTC that restricted the cable deformation. When the load was 2000 kN, the plotting points were one less than the other cases. The main reason is that the strain gauge at the loading end was damaged when the load increased from 1600 to 2000 kN. Thus, the strain gauge could not collect valid data.

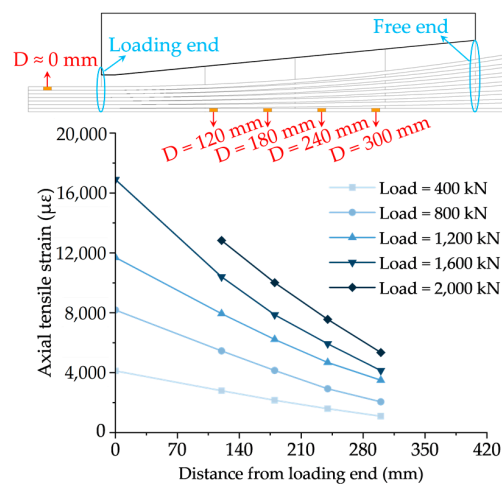


**Figure 16.** Axial tensile strains of T-1 at different load grades.

Based on the measured tensile strains in Figure 16, the mean shear stress of T-1 was calculated using the formula proposed in a previous study [27]. In this formula, the mean axial tensile strain, distance between two adjacent SGs, and elastic modulus of the BFRP tendons are considered. As shown in Figure 17, when the load was less than 1200 kN, the mean shear stress decreased gradually from the loading end to the free end. This phenomenon can be attributed to the varying elastic modulus of the LTC and the relatively small wedge displacement. Additionally, the mean shear stress near the loading end decreased drastically when the load was greater than 1200 kN. This phenomenon is possibly caused by the excessive wedge displacement (radial extrusion) of the LTC that limits its axial tensile deformation and the measuring error of the SGs. In general, no shear stress concentration was observed in the anchoring zone, illustrating that the variable-stiffness design for the LTC was beneficial for reducing the stress concentration caused by the excessive stiffness in the loading-end LTC.

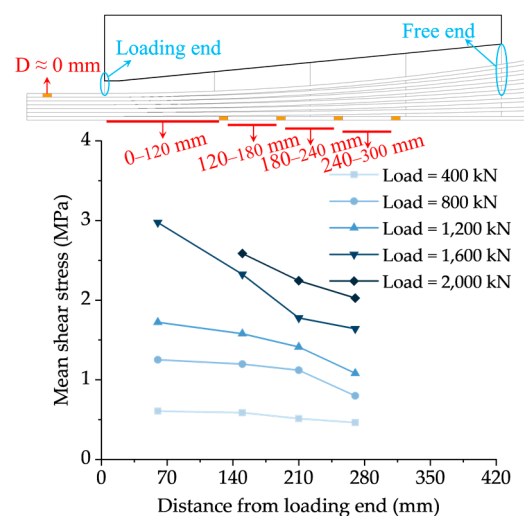


Figure 17. Mean shear stress of T-1 at different load grades.

## 5. Contribution of the Research to Practical Implementation

The research contribution mainly proposes a simplified model for anchoring design, cable manufacturing, and performance verification. Generally, the optimization design for anchoring cable is the premise of cable preparation. For different FRP cables, a simplified simulation method with high accuracy and efficiency can shorten the development cycle of FRP CAS. Based on the designed FRP CAS, the developed manufacturing method in the laboratory can provide helpful preparation strategies and details for actual factory production. The large-diameter BFRP cable in this paper was verified to be high anchoring efficiency. Furthermore, the anchoring efficiency of the cable may be further improved by optimizing the anchoring system. The design and testing results show that the BFRP cable is capable of engineering application. The cost-effective BFRP cables will also be a solid complement to the CFRP cables in the future. Thus, it is necessary to carry out in-depth scientific research on BFRP cables.

## 6. Conclusions

The main conclusions are as follows.

Compared with the full model, the simplified model has apparent advantages in terms of the decrease in element number, increase in computing efficiency, and convergence. The simulated results of the simplified dispersed-tendon model established using the concentric ring simplification method can be corrected by dividing the revised compensation factor from the geometric relations among the tendons.

The FE results showed that the loading-end radial stress decreased by 12% when the tendon spacing decreased from 1.5 mm to 0. Meanwhile, the tensile stress difference

between the inside and outside of the tendons decreased by 38%. The radial compressive stress of the cable and the shear stress of the LTC in the dispersed-tendon CAS were lower than those in the parallel-tendon CAS when the same cable was anchored. In addition, the loading ends of the cable and LTC were verified as the maximum stress positions.

The experimental load–displacement relationship and axial displacement agreed well with the simulated results. All tendons were completely ruptured in the testing section, and the LTC was nearly unchanged. The ultimate tensile force of the cable was 2419 kN, and the corresponding anchoring efficiency was 93%. The axial tensile strain of the anchoring-zone cable generally decreased at a rate of 10–43  $\mu\epsilon/m$  when the load increased from 400 to 2000 kN. The shear stress concentration of the cable in the anchoring zone can be eliminated by applying a variable-stiffness LTC.

In general, a novel dispersed-tendon CAS for large-diameter BFRP cables was developed based on a previously developed LTC. The static behaviors of the CAS were then numerically evaluated using a simplified 3D FE model and implemented in a full-scale experiment. The shortcomings of the simplified model will be further overcome by releasing the circumferential stress of the anchor-zone cable. The developed large-diameter BFRP cable CAS is the foundation for further promotion and application.

**Author Contributions:** Conceptualization, X.W.; methodology, J.Z., L.D. and S.L.; software, J.Z.; validation, J.Z. and X.W.; formal analysis, J.Z. and L.D.; investigation, J.Z., L.D. and S.L.; resources, X.W.; data curation, J.Z.; writing—original draft preparation, J.Z.; writing—review and editing, J.Z. and X.W.; supervision, Z.W.; project administration, J.Z. and X.W.; funding acquisition, X.W. All authors have read and agreed to the published version of the manuscript.

**Funding:** The research was funded by the National Natural Science Foundation of China (Grant 52208233 & 52278244), the Natural Science Foundation of Jiangsu Province (Grant No. BK20220855), the China Postdoctoral Science Foundation (Grant No. 2022M720726), the Excellent Postdoctoral Program of Jiangsu Province (Grant No. 2022ZB132), and the National Key Research and Development Program of China (No. 2022YFB3706503).

**Data Availability Statement:** The data presented in this study are available on request from the corresponding author.

**Acknowledgments:** The authors also acknowledge Jiangsu Green Materials Valley New Material T&D Co., Ltd. for providing BFRP tendons.

**Conflicts of Interest:** The authors declare no conflict of interest.

## References

1. Wang, Q.; Zhu, H.; Zhang, B.; Tong, Y.; Teng, F.; Su, W. Anchorage systems for reinforced concrete structures strengthened with fiber-reinforced polymer composites: State-of-the-art review. *J. Reinf. Plast. Comp.* **2020**, *39*, 327–344. [[CrossRef](#)]
2. Feng, B.; Wang, X.; Wu, Z.; Yang, Y.; Pan, Z. Performance of anchorage assemblies for CFRP cables under fatigue loads. *Structures* **2021**, *29*, 947–953. [[CrossRef](#)]
3. Xie, G.H.; Tao, Z.; Wang, C.; Yan, P.; Liu, Y. Prediction of Elastic-Softening-Debonding behavior for CFRP Tendon-Adhesively bonded anchors. *Structures* **2022**, *40*, 659–666. [[CrossRef](#)]
4. Meier, U.; Farshad, M. Connecting high-performance carbon-fiber-reinforced polymer cables of suspension and cable-stayed bridges through the use of gradient materials. *J. Comput.-Aided Mater. Des.* **1996**, *3*, 379–384. [[CrossRef](#)]
5. Wang, X.; Wu, Z.; Wu, G.; Zeng, F. Enhancement of basalt FRP by hybridization for long-span cable-stayed bridge. *Compos. Part B Eng.* **2013**, *44*, 184–192. [[CrossRef](#)]
6. Shi, J.; Wang, X.; Wu, Z.; Zhu, Z. Optimization of anchorage and deviator for concrete beams prestressed with external fiber-reinforced polymer tendons. *Compos. Struct.* **2022**, *297*, 115970. [[CrossRef](#)]
7. Liu, Y.; Zwingmann, B.; Schlaich, M. Carbon fiber reinforced polymer for cable structures—A review. *Polymers* **2015**, *7*, 2078–2099. [[CrossRef](#)]
8. Wang, L.; Zhang, J.; Xu, J.; Han, Q. Anchorage systems of CFRP cables in cable structures—A review. *Constr. Build. Mater.* **2018**, *160*, 82–99. [[CrossRef](#)]
9. Zhao, J.; Mei, K.; Wu, J. Long-term mechanical properties of FRP tendon-anchor systems—A review. *Constr. Build. Mater.* **2020**, *230*, 117017. [[CrossRef](#)]
10. Schlaich, M.; Liu, Y.; Zwingmann, B. Carbon Fiber Reinforced Polymer for Orthogonally Loaded Cable Net Structures. *Struct. Eng. Int.* **2015**, *25*, 34–42. [[CrossRef](#)]

11. Mei, K.; Seracino, R.; Lv, Z. An experimental study on bond-type anchorages for carbon fiber-reinforced polymer cables. *Constr. Build. Mater.* **2016**, *106*, 584–591. [[CrossRef](#)]
12. Xie, G.; Yin, J.; Liu, R.; Chen, B.; Cai, D. Experimental and numerical investigation on the static and dynamic behaviors of cable-stayed bridges with CFRP cables. *Compos. Part B Eng.* **2017**, *111*, 235–242. [[CrossRef](#)]
13. Meier, U.; Winistorfer, A.; Haspel, L. Reinforced polymer hangers world's first large bridge fully relying on carbon fiber reinforced polymer hangers. *SAMPE J.* **2021**, *57*, 22–30.
14. Ai, P.; Feng, P.; Lin, H.; Zhu, P.; Ding, G. Novel self-anchored CFRP cable system: Concept and anchorage behavior. *Compos. Struct.* **2021**, *263*, 113736. [[CrossRef](#)]
15. Fang, Z.; Wang, C.; Zhang, H.; Zhang, K.; Xiang, Y. Experimental study on anchoring performance of CFRP strand in reactive power concrete. *China J. Highw. Transport.* **2016**, *29*, 198–206.
16. Yang, D.; Zhang, J.; Song, S.; Zhou, F.; Wang, C. Experimental investigation on the creep property of carbon fiber reinforced polymer tendons under high stress levels. *Materials* **2018**, *11*, 2273. [[CrossRef](#)]
17. Feng, B.; Wang, X.; Wu, Z. Evaluation and prediction of carbon fiber-reinforced polymer cable anchorage for large capacity. *Adv. Struct. Eng.* **2019**, *22*, 1952–1964. [[CrossRef](#)]
18. Song, S.; Zang, H.; Duan, N.; Jiang, J. Experimental research and analysis on fatigue life of carbon fiber reinforced polymer (CFRP) tendons. *Materials* **2019**, *12*, 3383. [[CrossRef](#)]
19. Kim, T.; Jung, W. Improvement of anchorage performance of carbon fiber-reinforced polymer cables. *Polymers* **2022**, *14*, 1239. [[CrossRef](#)]
20. Yang, Y.; Fahmy, M.; Guan, S.; Pan, Z.; Zhan, Y.; Zhao, T. Properties and applications of FRP cable on long-span cable-supported bridges: A review. *Compos. Part B Eng.* **2020**, *190*, 107934. [[CrossRef](#)]
21. Shi, J.; Wang, X.; Wu, Z.; Zhu, Z. Creep behavior enhancement of a basalt fiber-reinforced polymer tendon. *Constr. Build. Mater.* **2015**, *94*, 750–757. [[CrossRef](#)]
22. Peng, Z.; Wang, X.; Wu, Z. A bundle-based shear-lag model for tensile failure prediction of unidirectional fiber-reinforced polymer composites. *Mater. Des.* **2020**, *196*, 109103. [[CrossRef](#)]
23. Shi, J.; Wang, X.; Wu, Z.; Wei, X.; Ma, X. Long-term mechanical behaviors of uncracked concrete beams prestressed with external basalt fiber-reinforced polymer tendons. *Eng. Struct.* **2022**, *262*, 114309. [[CrossRef](#)]
24. Wang, X.; Shi, J.; Liu, J.; Yang, L.; Wu, Z. Creep behavior of basalt fiber reinforced polymer tendons for prestressing application. *Mater. Des.* **2014**, *59*, 558–564. [[CrossRef](#)]
25. Yang, Y.; Wang, X.; Wu, Z. Long-span cable-stayed bridge with hybrid arrangement of FRP cables. *Compos. Struct.* **2020**, *237*, 111966. [[CrossRef](#)]
26. Zhou, J.; Wang, X.; Peng, Z.; Wu, Z.; Zhu, Z. Failure mechanism and optimization of fiber-reinforced polymer cable-anchor system based on 3D finite element model. *Eng. Struct.* **2021**, *243*, 112664. [[CrossRef](#)]
27. Wang, X.; Xu, P.; Wu, Z.; Shi, J. A novel anchor method for multitendon FRP cable: Manufacturing and experimental study. *J. Compos. Constr.* **2015**, *19*, 04015010. [[CrossRef](#)]
28. Shi, J.; Wang, X.; Zhang, L.; Wu, Z.; Zhu, Z. Composite-wedge anchorage for fiber-reinforced polymer tendons. *J. Compos. Constr.* **2022**, *26*, 04022005. [[CrossRef](#)]
29. Zhou, J.; Wang, X.; Peng, Z.; Wu, Z.; Zhu, Z. Evaluation of a large-tonnage FRP cable anchor system: Anchorage design and full-scale experiment. *Eng. Struct.* **2022**, *251*, 113551. [[CrossRef](#)]
30. Zhou, J.; Wang, X.; Wu, Z.; Zhu, Z. A Large-tonnage high-strength CFRP cable-anchor system: Experimental investigation and FE study. *J. Compos. Constr.* **2022**, *26*, 04022053. [[CrossRef](#)]
31. Peng, Z.; Wang, X.; Zhou, J.; Wu, Z. Reliability assessment of fiber-reinforced polymer cable-anchorage system. *Compos. Struct.* **2021**, *273*, 114308. [[CrossRef](#)]
32. *Chinese Standard GB/T 3002-2013; Test Method for Basic Mechanical Properties of fiber Reinforced Polymer Bar.* Chinese Standard Press: Beijing, China, 2013.
33. Zhou, J.; Wang, X.; Peng, Z.; Wu, Z.; Wei, X. Enhancement of FRP cable anchor system: Optimization of load transfer component and full-scale cable experiment. *J. Compos. Constr.* **2022**, *26*, 04022008. [[CrossRef](#)]
34. Wang, X.; Xu, P.; Wu, Z.; Shi, J. A novel anchor method for multi-tendon FRP cable: Concept and FE study. *Compos Struct.* **2015**, *120*, 552–564. [[CrossRef](#)]
35. *Chinese Standard T/CECS 10112-2020; Anchorage and Grip for Prestressing Fiber-Reinforced Polymer.* Chinese Standard Press: Beijing, China, 2020.

**Disclaimer/Publisher's Note:** The statements, opinions and data contained in all publications are solely those of the individual author(s) and contributor(s) and not of MDPI and/or the editor(s). MDPI and/or the editor(s) disclaim responsibility for any injury to people or property resulting from any ideas, methods, instructions or products referred to in the content.